R-44-006-001

An EPR Investigation of the Dynamic Jahn-Teller Effect in $SrCl_2:Y^{2+}$ and $SrCl_2:Sc^{2+}$

J. R. Herrington*† and T. L. Estle*

Physics Department, Rice University, Houston, Texas 77001

and

L. A. Boatner

Advanced Technology Center, Inc.‡, Dallas, Texas 75222

ABSTRACT

EPR spectra have been observed for $SrCl_2:Y^{2+}$ and $SrCl_2:Sc^{2+}$ at liquid helium temperatures. At 1.2K the spectra were dominated by anisotropic hyperfine patterns whose lineshapes and angular dependences were explained using second-order solutions of the effective Hamiltonian for an isolated ^2E_g state split by large random internal strains. Pronounced asymmetries in some of the strain-produced lineshapes for $SrCl_2:Sc^{2+}$ are shown to result from second-order terms in the solution of the effective Hamiltonian. Coexisting with the anisotropic hyperfine patterns are weak nearly isotropic hyperfine patterns with typical lineshapes. Variations in the apparent intensity of lines in these weak hyperfine patterns

* Work supported by the National Science Foundation and the National Aeronautics and Space Administration

† Presently at the Institut für Angewandte Festkörperphysik der Fraunhofer Gesellschaft, 78 Freiburg i. Br., West Germany

‡ Formerly LTV Research Center

as functions of the applied-magnetic-field direction and temperature imply that these lines result from averaging by vibronic relaxation of a portion of thé anisotropic pattern. This interpretation is further strengthened in the case of $SrCl_2:Sc^{2+}$ by the observation of a predicted anisotropy in the "averaged" spectrum. The effective Hamiltonian parameters for $SrCl_2:La^{2+}$, $SrCl_2:Y^{2+}$, and $SrCl_2:Sc^{2+}$ are analyzed in terms of crystal-field theory modified to include a weak to moderate vibronic interaction, i.e. a dynamic Jahn-Teller effect.

I. INTRODUCTION

For a nonlinear polyatomic complex Jahn and Teller[1] have shown that the orbital electronic degeneracy permitted by a symmetric nuclear configuration is incompatible with the stability of the symmetric configuration since asymmetric distortions remove the degeneracy and lower the energy of the system. For high symmetry complexes in solids, e.g. ions with a d^1 configuration in eight coordinated cubic sites, this instability is a result of the interaction between lattice vibrations and the electrons located on the ions. This vibrational-electronic or vibronic interaction determines the nature and the degeneracies of the states of the complex, both of which will generally be different from the results for the electronic states in the absence of the vibronic interaction. This subject has been extensively investigated theoretically[2-4]. When sufficiently strong, the vibronic interaction together with internal strains can produce a stable spontaneous distortion of the nuclear configuration to a symmetry sufficiently low to remove all orbital degeneracy, i.e. a "static" Jahn-Teller effect. However, even when the vibronic interaction is relatively weak, it produces pronounced effects on the matrix elements of certain vibronic operators and hence on certain experimental parameters, i.e. a "dynamic" Jahn-Teller effect. Since the existence of a significant vibronic interaction invalidates the

crystal field model, most experimental investigations have been directed toward finding instances where crystal field theory could not explain the observations. Ham[4] and Sturge[5] have reviewed all but the more recent experimental and theoretical developments in the study of the Jahn-Teller effect.

For orbital doublets only a limited amount of experimental data exists which permits definite inferences concerning the magnitude and nature of the vibronic coupling. This, together with the absence of systematic investigations and the restricted role experiment has played in verifying the substantial theoretical work, suggests the need for a more extensive experimental study of the Jahn-Teller effect and its implications concerning ^2E states.

In our previous work[6-9] concerning $SrCl_2:La^{2+}$ we have demonstrated that the ground vibronic state is an isolated doublet transforming like the $E_g(\Gamma_3^+)$ irreducible representation of O_h. This result, together with the observation that certain parameters were reduced from values predicted by crystal-field theory (i.e. zero vibronic coupling), implied that the weak to moderate vibronic-coupling model developed extensively by Ham[3,4] provided an accurate description of the $SrCl_2:La^{2+}$ system. This paper describes further EPR investigations of ions with ^2E_g ground states. We report here our studies of $SrCl_2:Y^{2+}$ and $SrCl_2:Sc^{2+}$ which were the subject of a previous preliminary presentation[10].

II. THEORY

The effective Hamiltonian formalism for an isolated vibronic doublet has been developed and solved to first order by Ham[3,4]. The importance of second-order terms in explaining EPR spectra was discussed previously in Ref. 8) (hereafter referred to as I). In this section the effective Hamiltonian will be reviewed and the solutions[8] will be used as a starting point for discussions of lineshapes and anisotropies of the EPR transitions observed for Sc^{2+} and Y^{2+} in $SrCl_2$.

The effective Hamiltonian for an isolated ^2E_g state[3,4,8,9] in O_h symmetry is given in Eq. (1).

$$
\begin{aligned}
H = {} & qV_s\,(e_\theta \mathcal{E}_\theta + e_\epsilon \mathcal{E}_\epsilon) + g_1\mu_B \vec{H}\cdot\vec{S}\,\mathcal{A}_1 + A_1\,\vec{I}\,\vec{S}\,\mathcal{A}_1 \\
& + \tfrac{1}{2}\,qg_2\mu_B[(3H_zS_z - \vec{H}\cdot\vec{S})\,\mathcal{E}_\theta + \sqrt{3}(H_xS_x - H_yS_y)\,\mathcal{E}_\epsilon] \\
& + \tfrac{1}{2}\,qA_2[3I_zS_z - \vec{I}\cdot\vec{S})\,\mathcal{E}_\theta + \sqrt{3}(I_xS_x - I_yS_y)\,\mathcal{E}_\epsilon] \\
& + \tfrac{1}{2}\,qQ[(3I_zI_z - \vec{I}\cdot\vec{I})\,\mathcal{E}_\theta + \sqrt{3}(I_xI_x - I_yI_y)\,\mathcal{E}_\epsilon] \qquad (1)
\end{aligned}
$$

The first term in the Hamiltonian represents the effects of internal strain or applied stress while the second and third terms are the isotropic Zeeman and hyperfine interactions. The last three terms are the anisotropic Zeeman, anisotropic hyperfine, and quadrupole interactions respectively. The quadrupole interaction has been

treated elsewhere[9]. The coupling coefficients qV_s, $g_1\mu_B$, A_1, $\frac{1}{2}qg_2\mu_B$, $\frac{1}{2}qA_2$, and $\frac{1}{2}qQ$ in Eq. (1) represent the relative strengths of the different terms with the reduction factor[3,4] included explicitly. The quantities $\vec{H}$, $\vec{S}$, and $\vec{I}$ are respectively the applied magnetic field, the electronic spin operator, and the nuclear spin operator. The components of strain e_θ and e_ϵ are defined as $e_\theta = \frac{1}{2}(2e_{zz} - e_{xx} - e_{yy})$ and $e_\epsilon = \frac{1}{2}\sqrt{3}(e_{xx} - e_{yy})$ where e_{xx}, e_{yy}, and e_{zz} are the diagonal components of the strain tensor. Matrix representations of the vibronic operators $\mathcal{a}_1$, $\mathcal{E}_\theta$, and $\mathcal{E}_\epsilon$ are given in Eq. (2). (Note the upper right hand matrix elements are $\langle\theta|\mathcal{O}|\epsilon\rangle$ where $|\theta\rangle$ and $|\epsilon\rangle$ are vibronic basis functions which transform like the $\theta(3z^2 - r^2)$ and $\epsilon(\sqrt{3}(x^2-y^2))$ components of the E_g irreducible representation of the point group O_h.)

$$\mathcal{a}_1 = \begin{pmatrix} 1 & 0 \\ 0 & 1 \end{pmatrix}; \quad \mathcal{E}_\theta = \begin{pmatrix} -1 & 0 \\ 0 & 1 \end{pmatrix}; \quad \mathcal{E}_\epsilon = \begin{pmatrix} 0 & 1 \\ 1 & 0 \end{pmatrix} \tag{2}$$

Assuming that the strain determines the composition of vibronic states (see Appendices A and B of I and Section VII from Ham[3]) the following second-order solution is easily obtained for the frequencies of the $\Delta M_S = \pm 1$, $\Delta M_I = 0$ transitions:

$$h\nu_\pm = \left[g_1 \pm \frac{1}{2}qg_2f_1 + \frac{(qg_2)^2}{g_1}f_3\right]\mu_B H + \left[A_1 \pm \frac{1}{2}qA_2f_1 + \frac{(qA_2)^2}{A_1}f_3 + 2\frac{qg_2}{g_1}qA_2f_3 + \frac{4(qQ)^2}{A_1}\left\{(f_3-f_4) + 2(f_4-2f_3)\,I(I+1)\right\}\right]M_I$$

$$+\left[\frac{(A_1 \mp \frac{1}{4} qA_2 f_1)^2}{2g_1\mu_B H} + \frac{(qA_2)^2}{g_1\mu_B H} f_4\right]\left[(I(I+1) - M_I^2\right]$$

$$+ \frac{(qA_2)^2}{g_1\mu_B H} f_3 M_I^2 + \frac{8(qQ)^2}{A_1} (2f_3 - f_4) M_I^3 \qquad (3)$$

The two signs refer to the two strain-produced Kramers doublets. The functions f_1, f_3 and f_4 are defined in Eqs. (4), (5), and (6).

$$f_1 = (3n^2-1)\cos\phi + \sqrt{3}(\ell^2-m^2)\sin\phi \qquad (4)$$

$$f_3 = \frac{1}{8}\left\{2 - \left[(3n^2-1)\cos\phi + \sqrt{3}(\ell^2-m^2)\sin\phi\right]^2 - \left[-(3n^2-1)\cos 2\phi + \sqrt{3}(\ell^2-m^2)\sin 2\phi\right]\right\} \qquad (5)$$

$$f_4 = \frac{1}{32}\left\{4 + \left[(3n^2-1)\cos\phi + \sqrt{3}(\ell^2-m^2)\sin\phi\right]^2 + 4\left[-(3n^2-1)\cos 2\phi + \sqrt{3}(\ell^2-m^2)\sin 2\phi\right]\right\} \qquad (6)$$

Here ℓ, m, and n represent the direction cosines of the magnetic field with respect to the cubic axes and $\tan\phi = e_\varepsilon/e_\theta$. The notation used here is the same as that used in I. Equations (5) and (6) are equivalent to the corresponding equations for f_3 and f_4 in I. The notation in Ref. 9) is somewhat different.

Using crystal field theory and assuming that the spin-orbit interaction is very small with respect to the cubic crystal-field interaction, i.e. $\lambda/\Delta \ll 1$, closed perturbation expressions may be derived for the parameters g_1, g_2, A_1, A_2 and Q in Eqs. (1) and (3).

These expressions are given in Eqs. (7-11) for a single d electron.

$$g_1 = 2.0023 - 4\lambda/\Delta \tag{7}$$

$$g_2 = -4\lambda/\Delta = g_1 - 2.0023 \tag{8}$$

$$A_1 = \frac{-2\mu_B\mu \langle r^{-3}\rangle}{I}\left[\kappa + \frac{4\lambda}{\Delta}\right] \tag{9}$$

$$A_2 = \frac{-2\mu_B\mu \langle r^{-3}\rangle}{I}\left[\frac{4}{7} + \frac{34\lambda}{7\Delta}\right] \tag{10}$$

$$Q = \frac{2e^2 Q_N}{7I(2I-1)} \langle r^{-3}\rangle \tag{11}$$

Here λ, Δ, μ_B, μ, I, $\langle r^{-3}\rangle$, κ, e, and Q_N are respectively, the spin-orbit coupling constant, the cubic crystal-field splitting 10 Dq, the Bohr magneton, the nuclear magnetic-dipole moment, the nuclear spin, the one-electron expectation value of r^{-3}, the Fermi contact parameter, the electron charge, and the nuclear electric-quadrupole moment. One immediately notes from Eqs. (9) and (10) that when κ is small, as it is for the $3d^1$ configuration, then $A_2 \tilde{-} A_1$, and terms in Eq. (3) of the form $(qA_2)^2/A_1$ are extremely important. These terms can have pronounced effects on the EPR lineshapes and will be discussed in greater detail for $SrCl_2:Sc^{2+}$ in Section IIIB.

As pointed out by Ham[3,4], rapid vibronic relaxation results in averaging of a portion of the stain-produced EPR lineshapes.

The first-order effects of such averaging on the EPR spectrum of $SrCl_2:La^{2+}$ were discussed in I and are illustrated schematically in Fig. 1a. If the relaxation rate τ^{-1} for the vibronic process is much greater than the difference between the two frequencies ν_+ and ν_- and both Kramers doublets are equally populated (i.e. the strain splitting δ satisfies $\delta \ll kT$), then an EPR signal will appear at the position $h\bar{\nu}$ given in Eq. (12).

$$h\bar{\nu} = \left(g_1 + \frac{(qg_2)^2}{g_1} f_3\right) \mu_B H + \left[A_1 + \frac{(qA_2)^2}{A_1} f_3 + \frac{2qg_2}{g_1} qA_2 f_3 + \frac{4(qQ)^2}{A_1}\left\{(f_3-f_4) + 2(f_4-2f_3)\, I(I+1)\right\}\right] M_I + \left(\frac{A_1^2}{2g_1\mu_B H} + \frac{(qA_2 f_1)^2}{32 g_1 \mu_B H} + \frac{(qA_2)^2}{g_1\mu_B H} f_4\right)\left[I(I+1) - M_I^2\right] + \frac{(qA_2)^2}{g_1\mu_B H} f_3 M_I^2 + \frac{8(qQ)^2}{A_1}(2f_3 - f_4) M_I^3 \,. \qquad (12)$$

Equation (12) gives the average of $h\nu_+$ and $h\nu_-$ for a given value of H. When the second-order terms in Eq. (12) are negligible averaging by relaxation produces an isotropic hyperfine pattern, each component of which is located midway between the two extremes of the appropriate envelope. This situation is shown schematically in Fig. 1b and characterizes the case of $SrCl_2:La^{2+}$. If A_1 and A_2 are comparable, then the $\frac{(qA_2)^2}{A_1}$ term is important and the "averaged"

spectrum will be slightly anisotropic. This is the case for $SrCl_2:Sc^{2+}$ which will be discussed further in Section IIIB.

III. EXPERIMENTAL RESULTS AND DISCUSSION

Single crystals of $SrCl_2:Y$ and $SrCl_2:Sc$ were grown from the melt using a vertical Bridgman technique described in I. The dopants were introduced as YCl_3 and $ScCl_3$. Strong fluorescence was observed in the "as-grown" crystals using short-wavelength U.V. (λ = 2537 Å) excitation, but EPR was not observed until the crystals were reduced. Reduction resulted from exposure to γ-rays from a high flux Cs^{137} source ($\sim 10^7$ rads) or by heating in Sr vapor (590C for 15 min.). The radiation produced a deep red color in the $SrCl_2:Y$ crystals but $SrCl_2:Sc$ crystals remained colorless. Reduction in a Sr vapor produced a dark metallic sheen for both $SrCl_2:Y$ and $SrCl_2:Sc$ crystals similar to that observed for $SrCl_2:La^{2+}$.

EPR spectra were observed using a back-reflection homodyne spectrometer operating at about 9 GHz. Precise orientations were obtained using independent orthogonal rotations of both the applied magnetic field and the crystal.

A. $SrCl_2:Y^{2+}$

The EPR spectrum observed at 1.2K for a reduced $SrCl_2:Y$ single crystal is shown in Fig. 2 for the applied magnetic field

parallel to the ⟨100⟩, ⟨111⟩, and ⟨110⟩ crystallographic directions. This spectrum is simpler than that of $SrCl_2:La^{2+}$ in I because the nuclear spin for the 100% naturally abundant isotope ^{89}Y is $\frac{1}{2}$.

The spectrum consists basically of two overlapping envelopes of transitions, each with the lineshape characteristic of random internal strains[3,4]. A schematic diagram of these two overlapping envelopes is shown in Fig. 3a. The dotted curve represents one of the envelopes ($M_I = -\frac{1}{2}$) and the dashed curve represents the other ($M_I = +\frac{1}{2}$). The curves were calculated for $\vec{H} \parallel \langle 100 \rangle$ using Eq. (3) and the parameters listed in Table 1 for $SrCl_2:Y^{2+}$. Each value of Ø was assumed to occur with equal probability thus producing two delta function lines (one for the upper sign and one for the lower sign in Eq. (3)). The solid curve is the sum of the dotted and dashed curves. The extremes of the two envelopes (located by small vertical bars below the curves) are the field positions predicted by Eq. (3) for Ø = 0°. The primary effect of considering each line to have a nonzero width is to broaden the extremes as shown in I. In Fig. 3b the observed first-derivative presentation of absorption versus magnetic field is shown for $\vec{H} \parallel \langle 100 \rangle$. The evaluation of the coupling coefficients g_1, qg_2, A_1, and qA_2 in Eq. (3) (note that the quadrupole interaction vanishes for $I = \frac{1}{2}$) is simplified for $\vec{H} \parallel \langle 100 \rangle$ since $f_3 = 0$ and $f_4 = 0$ at the extremes. A first-order estimate of these parameters can be easily obtained

using Eqs. (13-16) and the measured field position of the four peaks shown in Fig. 3b and labeled H_1, H_2, H_3, and H_4.

$$g_1 = \frac{\frac{\nu}{c}}{(H_1+H_2)\ \mu_B/hc} + \frac{\frac{\nu}{c}}{(H_3+H_4)\ \mu_B/hc} \tag{13}$$

$$qg_2 = -\frac{\frac{\nu}{c}}{(H_1+H_2)\ \mu_B/hc} + \frac{\frac{\nu}{c}}{(H_3+H_4)\ \mu_B/hc} \tag{14}$$

$$A_1(cm^{-1}) = -\left[\frac{H_1-H_2}{H_1+H_2} + \frac{H_3-H_4}{H_3+H_4}\right]\frac{\nu}{c} \tag{15}$$

$$qA_2(cm^{-1}) = \left[\frac{H_1-H_2}{H_1+H_2} - \frac{H_3-H_4}{H_3+H_4}\right]\frac{\nu}{c} \tag{16}$$

A more accurate set of parameters is obtained when the field positions H_1 to H_4 are modified to allow for second-order terms. In addition, corrections for the nonzero width of the individual resonances, following the prescription in I, are required. The iteratively refined values for these four parameters are listed in Table 1 and were used in Eq. (3) to compute the angular dependence of the extremes. These computed extremes are plotted as solid lines in Fig. 4. The open circles are the experimental values obtained using magnetic-field positions of the peaks in the first-derivative presentation of absorption and correcting for component linewidth as discussed in I. The fit is excellent considering the uncertainty in positions of the true extremes of the envelopes.

As seen in Fig. 2a, a pair of lines which were isotropic to within experimental error were observed to coexist with the anisotropic pattern discussed above. These lines increased in apparent intensity (the peak-to-peak amplitude in a first-derivative presentation) as the applied magnetic field was rotated in a $\{110\}$ plane toward a $\langle 111 \rangle$ direction. This angular variation in the intensities of these lines suggests that they result from averaging of a portion of the anisotropic pattern. As the temperature was increased, the intensities of these lines increased and the peaks in the first-derivative presentation of the anisotropic pattern broadened, again suggesting averaging by vibronic relaxation. The temperature dependence of the EPR spectrum for $\vec{H} \parallel \langle 100 \rangle$ is shown in Fig. 5. The approximately linear increase with temperature of the intensities of these two lines implies that the vibronic relaxation rate, τ^{-1}, is also increasing approximately linearly with temperature (characteristic of the direct process). This behavior was also observed for $SrCl_2:La^{2+}$ (see I).

The features discussed above were generally independent of incident microwave power, but a large number of anisotropic lines which saturated easily were also observed (see Fig. 2c in particular). Due to their saturation behavior, these lines were not associated with isolated Y^{2+} and, therefore, were not analyzed.

B. $SrCl_2:Sc^{2+}$

The EPR spectrum observed at 4.2K for a reduced $SrCl_2$:Sc single crystal is shown in Fig. 6 for the applied magnetic field parallel to the ⟨100⟩, ⟨111⟩, and ⟨110⟩ crystallographic directions. The dominant pattern is composed of eight anisotropic hyperfine envelopes since the nuclear spin of the 100% naturally abundant isotope ^{45}Sc is $\frac{7}{2}$. In Fig. 6 the extremes for the envelopes are indicated by small vertical bars below each trace. The coupling coefficients g_1, qg_2, A_1 and qA_2 were determined using the least squares procedure outlined in I and the spectrum obtained for $\vec{H} \parallel \langle 100 \rangle$. The values of these parameters are listed in Table 1. The quadrupole coupling parameter qQ was evaluated from the $\Delta M_I = \pm 1$ transitions for $\vec{H} \parallel \langle 111 \rangle$ as described previously[18]. These parameters were then used in Eq. (3) to compute the angular dependence of the extremes for each envelope. These calculated extremes are shown as solid lines in Fig. 7. The open circles designate the measured extremes. The weak lines located approximately midway between adjacent hyperfine lines for $\vec{H} \parallel \langle 111 \rangle$ (see Fig. 6b) are the $\Delta M_I = \pm 1$ "forbidden" transitions[18].

A careful examination of Fig. 6c, i.e. $\vec{H}$ ⟨110⟩, reveals pronounced asymmetries of the envelopes, particularly those at the low-field end. For these envelopes the low field extremes are sharper than the high field extremes. This asymmetry was observed

to be largest for $\vec{H} \parallel \langle 110 \rangle$ and seemed to be entirely absent for $\vec{H} \parallel \langle 100 \rangle$. This behavior is a result of the $(qA_2)^2/A_1$ term discussed in Section II. The origin of this asymmetry is shown schematically in Fig. 7. The dashed curves locate the position of the median transition of each of the eight envelopes, i.e. $\phi = 90°$ for a $\{110\}$ plane. Half of the lines composing each envelope must lie between the appropriate dashed line and the high-field extreme of that envelope and half must lie between the dashed lines and the low-field extreme. Thus, one sees from the dashed lines in Fig. 7 that with $\vec{H} \parallel \langle 110 \rangle$ the low-field extreme should be much sharper than the high-field extreme for the lowest three envelopes. The asymmetry is a maximum for $\vec{H} \parallel \langle 110 \rangle$ and apparently absent for $\vec{H} \parallel \langle 100 \rangle$ because the function f_3 in Eq. (5) is zero for $\vec{H} \parallel \langle 100 \rangle$ and a maximum for $\phi = 90°$ when $\vec{H}$ is along $\langle 110 \rangle$.

The temperature dependence of a portion of the EPR spectrum for a reduced $SrCl_2$:Sc sample is shown in Fig. 8. Traces (a), (b), and (c) correspond to progressively increasing temperature. As the temperature increased from 4.2K, the anisotropic pattern was observed to broaden while a weak eight-line pattern emerged. The intensities of the components of this weak pattern (located by solid vertical lines in Fig. 8) increased approximately linearly with temperature whereas the peaks in the anisotropic pattern near the envelope extreme broadened with increasing temperature.

In addition, for a constant temperature the apparent intensity of each weak line increased as the applied magnetic field was rotated in a $\{110\}$ plane toward a $\langle 111 \rangle$ direction. These characteristics imply that the origin of the weak pattern is averaging of a portion of the anisotropic pattern by direct vibronic relaxation. This interpretation was further strengthened by the observation that the positions of these lines for $\vec{H} \parallel \langle 100 \rangle$ differed by a measurable amount from the position of the eight hyperfine lines observed for $\vec{H} \parallel \langle 111 \rangle$ (denoted in Fig. 8 by the broken vertical lines). In particular, for $\vec{H} \parallel \langle 100 \rangle$ these lines were located at positions halfway between the extremes (i.e. the dashed lines in Fig. 7). It is exactly this type of anisotropy (both in magnitude and sense) that is predicted by Eqs. (12) and (4-6) for $\vec{H} \parallel \langle 100 \rangle$ and $\vec{H} \parallel \langle 111 \rangle$. The observation of this anisotropy is additional evidence that averaging by rapid vibronic relaxation produces this weak pattern. These arguments are somewhat more complicated for $\vec{H}$ along directions other than $\langle 111 \rangle$ or $\langle 100 \rangle$. For these general directions the averaged line is distributed between the dashed and dotted lines in Fig. 7 in a manner which depends on the magnitude of the vibronic relaxation rate. For a small τ^{-1} only the lines corresponding to values of ϕ very close to 90° (the dashed lines in Fig. 7) will average. If τ^{-1} is much larger than the difference in frequency of the extremes, then all lines will be averaged. The dotted line

in Fig. 7 corresponds to the position of the average of the two lines located at the extremes, that is a value of $\emptyset$ very close to 0° or 180°.

We wish to emphasize two differences that exist between the EPR spectra observed for $SrCl_2:Sc^{2+}$ and $SrCl_2:Y^{2+}$. First, pronounced asymmetries which are present in the lineshapes for $SrCl_2:Sc^{2+}$ for certain orientations of the applied magnetic field were not observed for $SrCl_2:Y^{2+}$. Second, while the pattern produced by rapid vibronic relaxation for $SrCl_2:Y^{2+}$ was isotropic within experimental error, that observed for $SrCl:Sc^{2+}$ exhibited a characteristic anisotropy in the hyperfine splitting. These differences occur because qA_2 is comparable to A_1 for Sc^{2+}. These features, together with many other details of the angular dependence, the lineshapes, the forbidden hyperfine transitions, and the temperature dependence, are all consistent with the assumption of an isolated ^2E_g state.

IV. IMPLICATIONS OF THE VIBRONIC MODEL

The EPR spectra reported for $SrCl_2:La^{2+}$ in I and for $SrCl_2:Y^{2+}$ and $SrCl_2:Sc^{2+}$ in this paper have been analyzed in terms of an effective Hamiltonian representing various interactions for an isolated ^2E_g state. Such a state is predicted by crystal field

theory to be the orbital ground state for a d^1 configuration in eight-fold cubic coordination. Ham[3,4] has shown that the symmetry classification of the ground vibronic state for a weak to moderate vibronic interaction is also ^2E_g. The only evidence that a vibronic interaction exists in the weak- to moderate-vibronic-coupling approximation is furnished by the observation that certain parameters in the effective Hamiltonian are reduced from the values predicted by crystal field theory. It is the purpose of this section to demonstrate that a reduction of the effective Hamiltonian parameters does indeed occur for the three systems, $SrCl_2:La^{2+}$, $SrCl_2:Y^{2+}$, and $SrCl_2:Sc^{2+}$ and that the implied variations in the strength of the vibronic coupling are physically reasonable.

The reduction factor q included explicitly in the qg_2, qA_2, and qQ parameters may be estimated most easily from Eqs. (7) and (8) and the parameters g_1 and qg_2 listed in Table 1. The results of these estimates are shown in Table 2. As pointed out by Ham[3,4], the reduction factors can be correlated with the strength of the vibronic interaction. In particular, the smaller the reduction factor, the larger the ratio of the Jahn-Teller energy E_{JT} to the phonon energy $\hbar\omega$. Using the calculations of Longuett-Higgins et al.[2], estimates of the ratio $E_{JT}/\hbar\omega$ were made and are listed in Table 2. Using a value of 300 cm^{-1} for $\hbar\omega$ (the

approximate energy of the optical phonons in $SrCl_2$) the estimates of the vibronic coupling coefficients V_{JT} listed in Table 2 were made. From the relationship between the vibronic-coupling coefficient and the strain-coupling coefficient[4] estimates of V_s were made and multiplied by the appropriate reduction factors. These approximate results are listed in Table 2. The variations in q and the parameters $E_{JT}/\hbar\omega$, V_{JT}, and qV_s are reasonable in view of the radial extent of d-electron wavefunctions. A 3d electron should be less extended than a 4d or 5d electron and better shielded from its surroundings. Thus, an ion with an incomplete 3d shell should be less sensitive to motions of the ligands. The vibronic interaction should, therefore, be weaker for a 3d electron than for a 4d or 5d electron. In addition, although the ratio $E_{JT}/\hbar\omega$ changes by an order of magnitude, the strain coupling coefficient qV_s (see Table 2) changes only by an approximate factor of 2. Thus, strains on the order of 10^{-4} to 10^{-5} produce splittings of the ^2E_g state which are comparable for all three ions. These splittings are sufficiently small that the direct vibronic relaxation rate increases approximately linearly with temperature above 1.3K. The relaxation rate is proportional to δ^4, where δ is the strain splitting, and is therefore very sensitive to small variations in δ. In particular, the direct vibronic relaxation rates at T = 20K computed using δ = 0.7, 1.3, and 1.5 cm^{-1} (see Table 2) and the

speeds of sound for $SrCl_2$[11] imply that the temperature at which the EPR spectrum becomes dominated by the pattern produced by rapid vibronic relaxation differs for the three systems. Since τ^{-1} for $SrCl_2:Sc^{2+}$ is at least an order of magnitude less than that for $SrCl_2:La^{2+}$, the temperature at which the "averaged" spectrum appears is substantially higher for the Sc-doped crystal. For $SrCl_2:Y^{2+}$ the averaging is appreciable at 1.2K principally because the differences $\nu_+ - \nu_-$ for the "averaged" transitions are smaller than for Sc^{2+} and La^{2+}.

By dividing the parameters qg_2, qA_2, and qQ by the reduction factor q one obtains the parameter g_2, A_2 and Q which can be combined with g_1 and A_1 in Eqs. (7-11) to obtain estimates for the parameters Δ, μ, $\langle r^{-3} \rangle$, κ, and Q_N. These values are listed in Table 2. The systematic variations in Δ and $\langle r^{-3} \rangle$ are reasonable. The nuclear magnetic-dipole moments and nuclear electric-quadrupole moments agree well with the currently accepted values (shown in parentheses in Table 2).

The measured EPR parameters for $SrCl_2:La^{2+}$, $SrCl_2:Y^{2+}$, and $SrCl_2:Sc^{2+}$ are all consistent with the following model, which is illustrated in Fig. 9. In an eight-coordinated metal site the ^2D free-ion ground term of an ion with one d electron is split by the cubic crystal-field into a ground ^2E_g state and a $^2T_{2g}$ state separated by 10,000 cm^{-1} to 20,000 cm^{-1}. The ground vibronic state

resulting from a weak to moderate vibronic interaction ($E_{JT}/\hbar\omega \tilde{-}$ 0.1 to 1.0) is a ^2E_g state. The first excited state is on the order of 100 cm^{-1} above the ground state. Due to large random internal strains (on the order of 10^{-4} to 10^{-5}) the ^2E_g state is split into two Kramers doublets separated in energy by about 1 cm^{-1}. This strain splitting varies from site to site due to the distribution in strain magnitude. The Kramers degeneracy is removed by the applied magnetic field and the magnitude of the Zeeman splitting depends on the ratio of e_θ and e_ε strain components at each site and on the orientation of the applied magnetic field.

The EPR transitions (indicated by solid arrows in Fig. 9) consist of a complex envelope of transitions. The shape of this envelope results from the distribution in e_ε/e_θ. Due to vibronic relaxation (as indicated by wavy arrows in Fig. 9) a portion of the anisotropic spectrum averages to produce a weak nearly isotropic pattern at low temperatures. This pattern increases in intensity with increasing temperature. All features of the EPR spectrum, with the exception of a number of lines observed for $SrCl_2:Y^{2+}$ and not associated with Y^{2+} and a single line with g = 2 observed at high temperatures for Sc^{2+} in $SrCl_2$, are consistent with the description given above and are described within experimental error by an effective Hamiltonian for an isolated ^2E_g state.

V. SUMMARY

EPR spectra have been observed for $SrCl_2:Y^{2+}$ and $SrCl_2:Sc^{2+}$ at liquid helium temperatures. At 1.2K the spectra were dominated by anisotropic hyperfine patterns whose lineshapes and angular dependences were explained using second-order solutions of the effective Hamiltonian for an isolated ^2E_g state. Pronounced asymmetries in some of the lineshapes observed for $SrCl_2:Sc^{2+}$ result from second-order terms previously neglected in the lineshape analysis. The observed variations of the effective Hamiltonian parameters are physically reasonable.

Weak nearly-isotropic hyperfine lines were observed to coexist with the anisotropic patterns. Variations in the intensities of these weak lines as functions of temperature and magnetic-field orientation imply that they result from averaging of a portion of the anisotropic pattern by direct vibronic relaxation. Relaxation rates implied by this interpretation are consistent with those calculated from the strength of the vibronic interaction. This interpretation was further strengthened in the case of $SrCl_2:Sc^{2+}$ by the observation of a small predicted anisotropy.

In conclusion, essentially all features of the EPR spectra observed for $SrCl_2:La^{2+}$, $SrCl_2:Y^{2+}$, and $SrCl_2:Sc^{2+}$ are consistent with the model discussed previously and represented schematically

in Fig. 9. Observed reductions of certain parameters from the values predicted by crystal field theory imply the existence of a weak to moderate vibronic interaction, i.e. a dynamic Jahn-Teller effect.

ACKNOWLEDGMENTS

We gratefully acknowledge the valuable technical assistance of Mr. E. G. Clardy and the useful comments of B. Dischler on the manuscript. In addition we thank the Office of Naval Research for the contribution of helium used in the initial stages of this work.

TABLE 1

Effective Hamiltonian Parameters Measured for Sc^{2+}, Y^{2+}, and La^{2+} in $SrCl_2$

System	g_1	qg_2	A_1 ($\times 10^{-4} cm^{-1}$)	qA_2 ($\times 10^{-4} cm^{-1}$)	qQ ($\times 10^{-4} cm^{-1}$)
$SrCl_2:Sc^{2+}$	$+1.9531 \pm .0005$ [a]	$-0.0442 \pm .0005$ [a]	$-62.7 \pm .5$ [a]	$-31.5 \pm .5$ [a]	$-.20 \pm .05$ [b]
$SrCl_2:Y^{2+}$	$+1.9289 \pm .0005$ [a]	$-0.0478 \pm .0005$ [a]	$+24.3 \pm .5$ [a]	$+5.0 \pm .5$ [a]	---
$SrCl_2:La^{2+}$	$+1.8808 \pm .0005$ [c]	$-0.0687 \pm .0005$ [c]	$-119.5 \pm .5$ [c]	$-18.8 \pm .5$ [c]	$+.15 \pm .05$ [b]

The signs have been chosen consistent with predictions of crystal field theory and sign relations implied by the data analysis.

a) this paper

b) reference 9

c) reference 8

TABLE 2

Vibronic Model Parameters

Parameter	$SrCl_2:Sc^{2+}$	$SrCl_2:Y^{2+}$	$SrCl_2:La^{2+}$
q	.86	.65	.57
$E_{JT}/\hbar\omega$	0.1	0.5	1.0
$V_{JT}(cm^{-1})$	2000	5000	7000
$qV_s(cm^{-1})$	7000	13000	15000
$\delta(cm^{-1})$*	.7 to .07	1.3 to .13	1.5 to .15
$\tau^{-1}(sec^{-1})$‡	$5x10^8$	$4x10^9$	$9x10^9$
$\Delta(cm^{-1})$	10,000	15,000	20,000
μ(Nuclear magnetons)+	5(4.75)	-.2(-.14)	2.5(2.76)
$\langle r^{-3}\rangle(x10^{22}G^2/erg)$	.5	.6	.7
κ	1.0	2.0	2.5
Q_N(barns)+	-.3(-.22)	---	+.3(+.2)

* The first number is the strain splitting computed using a strain of 10^{-4} and the second is for a strain of 10^{-5}.

‡ T = 20K

+ numbers in parentheses are currently accepted values.

REFERENCES

1. H. A. Jahn and E. Teller, Proc. Roy. Soc. (London) A161, 220 (1937).

2. H. C. Longuett-Higgins, U. Öpik, M.H.L. Pryce, and R. A. Sack, Proc. Roy. Soc. (London) A244, 1 (1958).

3. F. S. Ham, Phys. Rev. 166, 307 (1968).

4. F. S. Ham, Electron Paramagnetic Resonance [ed. by S. Geschwind, Plenum Press, New York, 1971].

5. M. D. Sturge, Solid State Physics, Vol. 20 [ed. by F. Seitz, D. Turnbull, and H. Ehrenreich, Academic Press, New York and London, 1967].

6. L. A. Boatner, B. Dischler, J. R. Herrington, and T. L. Estle, Bull. Am. Phys. Soc. 14, 355 (1969).

7. J. R. Herrington, B. Dischler, T. L. Estle, and L. A. Boatner, Phys. Rev. Letters 24, 984 (1970).

8. J. R. Herrington, T. L. Estle, and L. A. Boatner, Phys. Rev. B 3, 2933 (1971).

9. J. R. Herrington, T. L. Estle, and L. A. Boatner, Bull. Am. Phys. Soc. 16, 387 (1971); Phys. Rev. B 5, 2500 (1972).

10. T. L. Estle, J. R. Herrington, and L. A. Boatner, Bull. Am. Phys. Soc. 16, 386 (1971).

11. H. V. Lauer, Jr., K. A. Solberg, D. H. Kuhner, and W. E. Bron, Phys. Letters 35A, 279 (1971).

FIGURE CAPTIONS

Fig. 1 (a) The lineshape in first order produced by the distribution in the angle ϕ given by $\tan\phi = e_\varepsilon/e_\theta$. EPR signals occur in pairs, equidistant from the center of the envelope.

(b) The effect of rapid vibronic relaxation is to average those pairs of transitions whose frequency differences ($\nu_+ - \nu_-$ of Eq. (3)) are less than the vibronic relaxation rate, τ^{-1}. Hence, as the relaxation rate increases with temperature, that portion of the envelope that is averaged increases. In addition, rotation of the magnetic field in a $\{110\}$ plane toward a $\langle 111\rangle$ axis reduces the value of the function f_1 to zero as shown in Eq. (4). Hence, as the field gets closer to a $\langle 111\rangle$ direction, more transitions satisfy the condition $\tau^{-1} > \nu_+ - \nu_-$ and the "averaged" line increases in intensity. The absorption is shown schematically as a function of applied magnetic field with the extremes of the envelope designated by vertical lines and labeled with effective first-order g factors.

Fig. 2 The angular dependence of the EPR spectrum observed for a reduced $SrCl_2$:Y single crystal; (a) $\vec{H} \parallel \langle 100 \rangle$, (b) $\vec{H} \parallel \langle 111 \rangle$, and (c) $\vec{H} \parallel \langle 110 \rangle$. The first derivative of absorption is shown versus magnetic field. Extremes of the two overlapping envelopes are identified by small vertical bars below each trace. The dashed vertical lines designate the positions of the two transitions for $\vec{H} \parallel \langle 111 \rangle$ and aid in identifying the lines produced by rapid vibronic relaxation. A large number of anisotropic lines, best seen for $\vec{H} \parallel \langle 110 \rangle$, were observed. These lines saturated easily and hence were not associated with the isolated Y^{2+} imperfections.

Fig. 3 (a) A schematic representation of the density of EPR transitions as a function of applied magnetic field. These were calculated using Eq. (3) assuming that all values of ϕ occur with equal probability. The dotted curve represents the $M_I = -\frac{1}{2}$ envelope and the dashed curve represents the $M_I = +\frac{1}{2}$ envelope. The solid curve results from adding the dashed and dotted curves. The envelope extremes are shown as small vertical bars below the curves.

(b) The first derivative presentation of absorption versus magnetic field observed for a reduced $SrCl_2$:Y single crystal. The dashed vertical lines locate the two lines produced by averaging a portion of the anisotropic pattern. The extremes of the two envelopes are shown as small vertical bars below the trace.

Fig. 4 The angular dependence of the extremes in the EPR spectrum observed for $SrCl_2:Y^{2+}$. The solid lines were calculated using Eq. (3) together with the parameters listed in Table 1 for $SrCl_2:Y^{2+}$. The open circles represent experimental measurements. The dashed lines indicate the location of the "averaged" lines.

Fig. 5 The temperature dependence of the EPR spectrum from a reduced $SrCl_2$:Y single crystal with $\vec{H} \| \langle 100 \rangle$, (a) 4.2K, (b) 3.2K, and (c) 1.6K. The dashed vertical lines identify the lines produced by averaging resulting from vibronic relaxation. The first derivative of absorption versus magnetic field is shown and the extremes for the two envelopes are designated by small vertical bars at the bottom of the figure.

Fig. 6 The angular dependence of the EPR spectrum observed for a reduced $SrCl_2$:Sc single crystal; (a) $\vec{H} \| \langle 100 \rangle$, (b) $\vec{H} \| \langle 111 \rangle$, and (c) $\vec{H} \| \langle 110 \rangle$. The first derivative of absorption versus magnetic field is shown. Extremes of the eight anisotropic envelopes are designated by small vertical bars below each trace. The dashed vertical lines denote the positions of the eight collapsed envelopes for $\vec{H} \| \langle 111 \rangle$. Note that they do not lie halfway between the two extremes for each envelope for $\vec{H} \| \langle 100 \rangle$. Note also the pronounced asymmetry of the lowest three envelopes of transitions for $\vec{H} \| \langle 110 \rangle$.

Fig. 7 The angular dependence of the extremes of the EPR spectrum observed for a reduced sample of $SrCl_2:Sc^{2+}$. The solid lines were computed using Eq. (3) together with the parameters listed in Table 1 for Sc^{2+}. The open circles represent the measured extremes. The dashed lines were calculated from Eq. (3) with the $SrCl_2:Sc^{2+}$ parameters assuming $\phi = 90°$. These dashed lines locate the position of the lines due to averaging by vibronic relaxation for a small relaxation rate. The dotted lines locate the positions of the lines produced by averaging the transitions at

the extremes of each envelope. The angular variation of the dashed and dotted lines are a result of the $(qA_2')^2/A_1$ second-order term in Eq. (3).

Fig. 8 The temperature dependence of a portion of the EPR spectrum observed for a reduced $SrCl_2:Sc^{2+}$ sample. The first derivative of absorption versus magnetic field is shown. The lines produced by rapid vibronic relaxation are identified by solid vertical lines. The broken vertical lines designate the positions of the transitions observed for $\vec{H} \| \langle 111 \rangle$. The extremes of each envelope are identified by small vertical bars at the bottom of the figure. The temperature is progressively increasing from (a) to (b) to (c) but values for the temperature were not obtained.

Fig. 9 The schematic energy level diagram implied by the interpretation of the EPR parameters. The ^2D free-ion term is split by the cubic crystal field into ^2E_g and $^2T_{2g}$ states with the ^2E_g lowest. A weak to moderate vibronic interaction results in a series of vibronic states such that the ground vibronic state is also a ^2E_g state. The first

excited vibronic state is sufficiently far from the ground state to enable one to treat the ground state as an isolated ^2E_g state. This state is split by random strains into two Kramers doublets. This splitting depends on the magnitude of the strain. The Kramers degeneracy is removed by an applied magnetic field and EPR transitions (represented by straight arrows) are induced by the microwave magnetic field. The wavy arrows represent transitions resulting from vibronic relaxation. They can produce an averaging of a portion of the anisotropic EPR pattern yielding nearly isotropic lines. This type of relaxation should not be confused with spin-lattice relaxation.

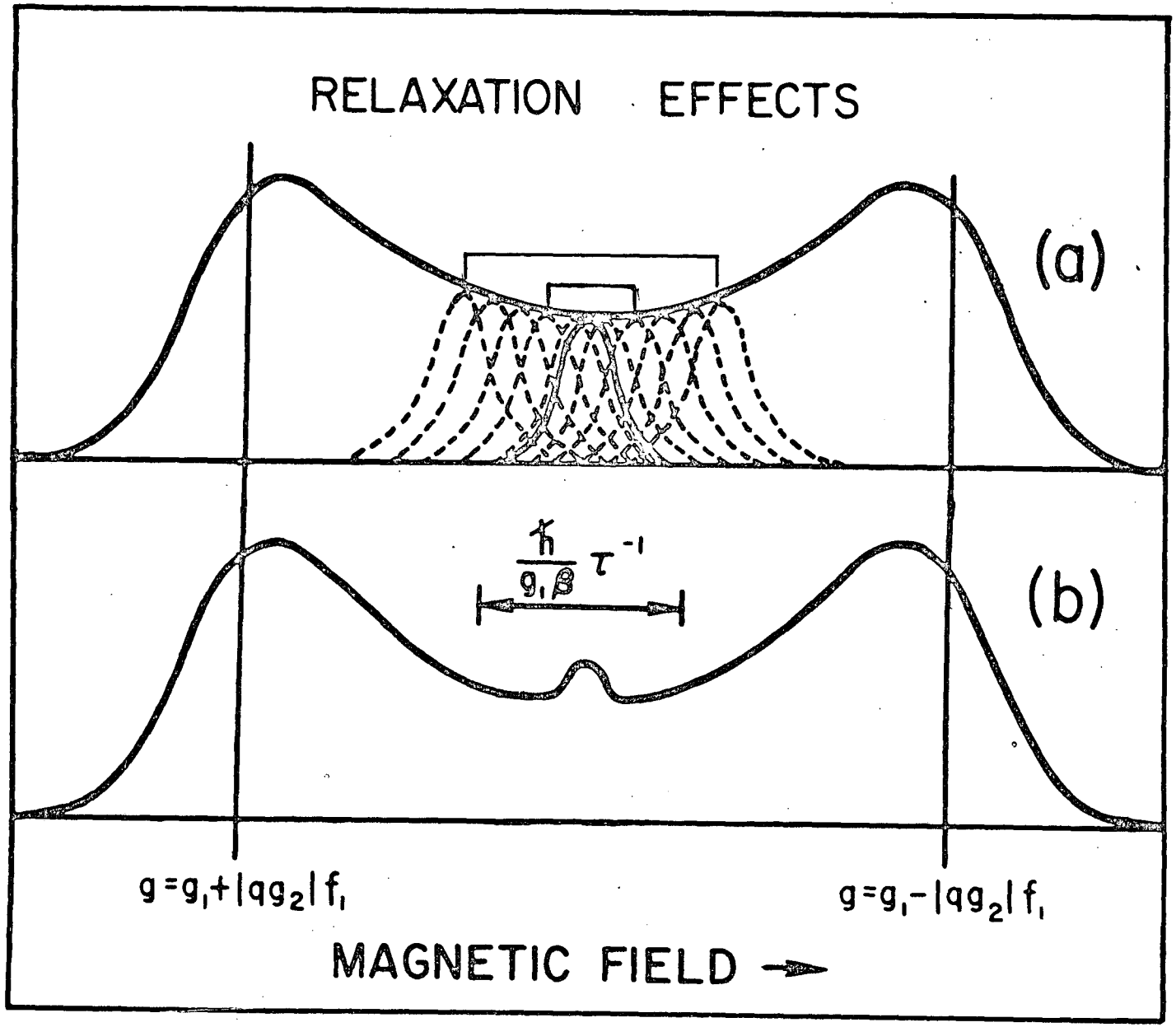
RELAXATION EFFECTS
(a)
(b)
$\frac{\hbar}{g_1\beta}\tau^{-1}$
$g=g_1+|qg_2|f_1$
$g=g_1-|qg_2|f_1$
MAGNETIC FIELD →

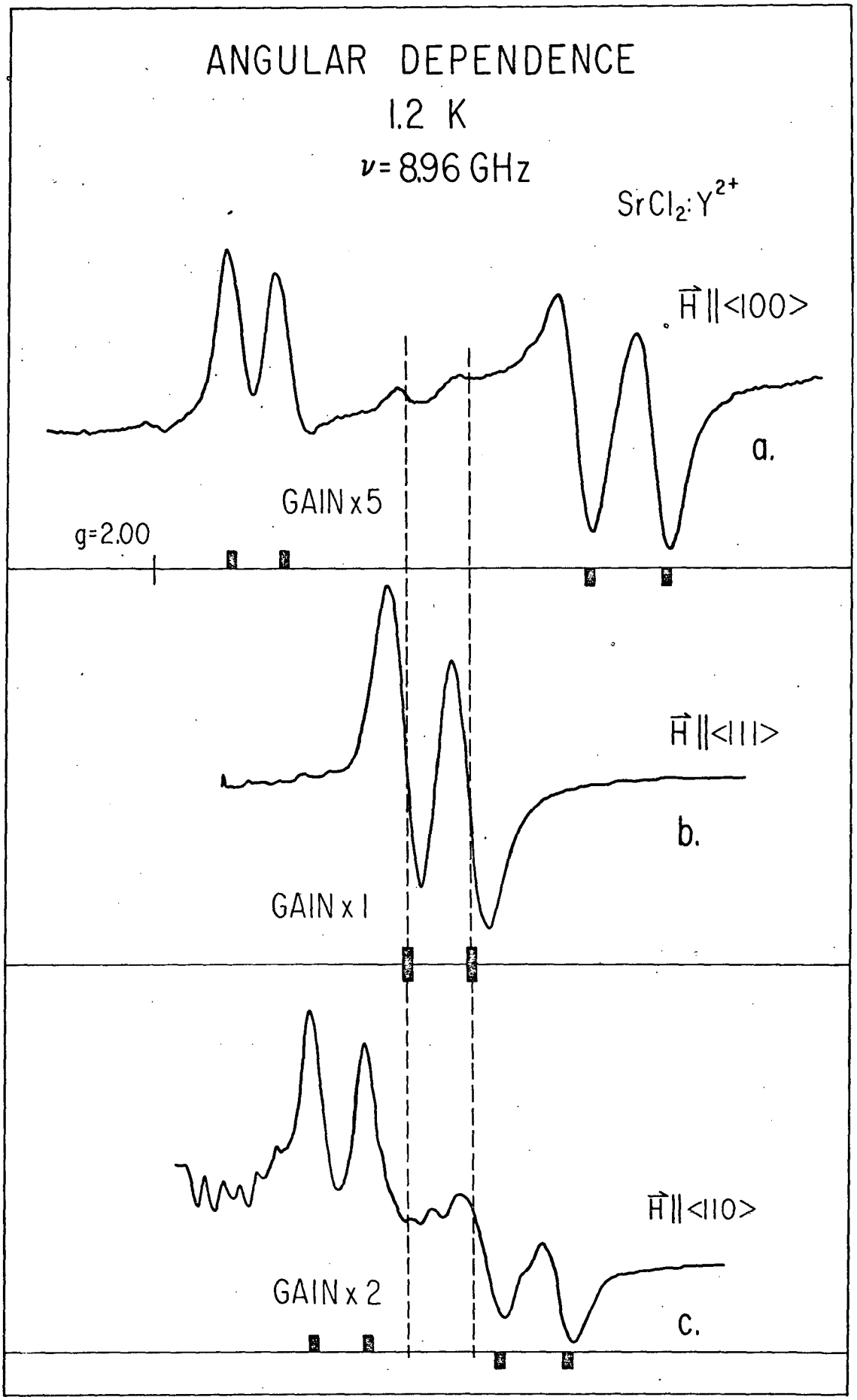
ANGULAR DEPENDENCE
1.2 K
ν = 8.96 GHz
SrCl2:Y2+
H ∥ <100>
a.
GAIN x 5
g=2.00
H ∥ <111>
b.
GAIN x 1
H ∥ <110>
GAIN x 2
c.
MAGNETIC FIELD →
40 GAUSS

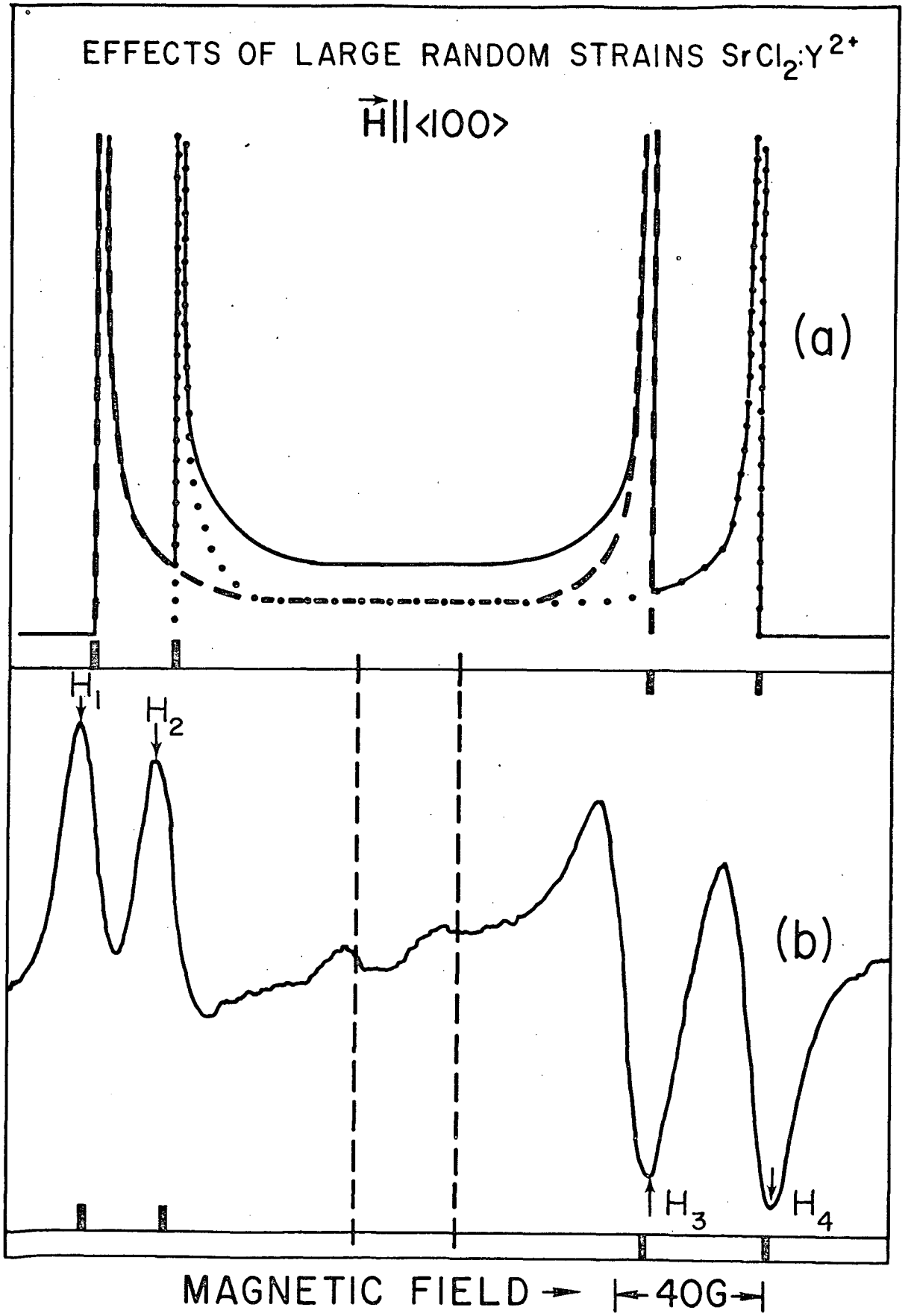
EFFECTS OF LARGE RANDOM STRAINS $SrCl_2:Y^{2+}$
$\vec{H} \| \langle 100 \rangle$
(a)
H_1
H_2
(b)
H_3
H_4
MAGNETIC FIELD → ←40G→

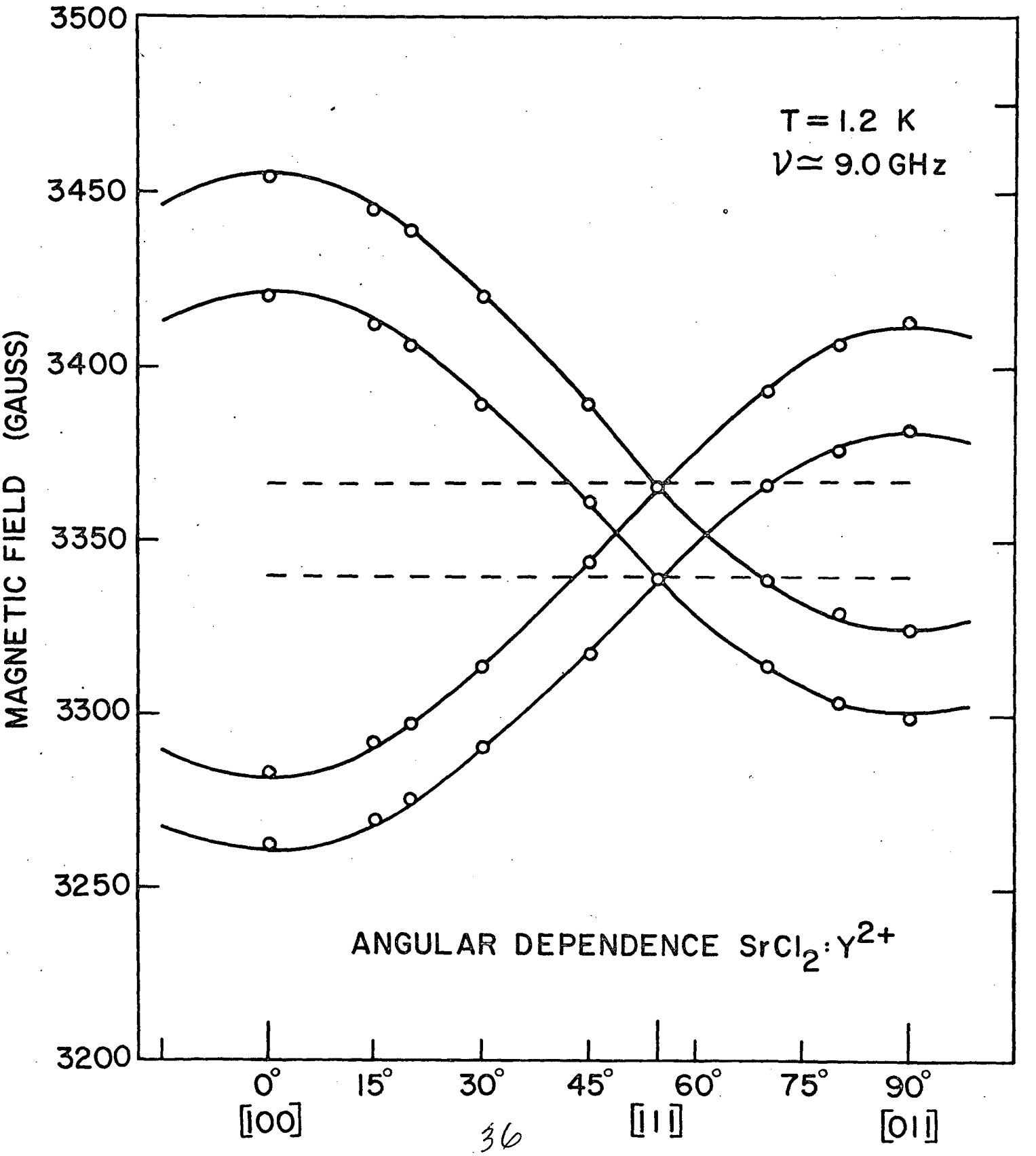
3500
3450
3400
3350
3300
3250
3200
MAGNETIC FIELD (GAUSS)
T = 1.2 K
ν ≃ 9.0 GHz
ANGULAR DEPENDENCE SrCl2:Y2+
0°
15°
30°
45°
60°
75°
90°
[100]
[11]
[011]

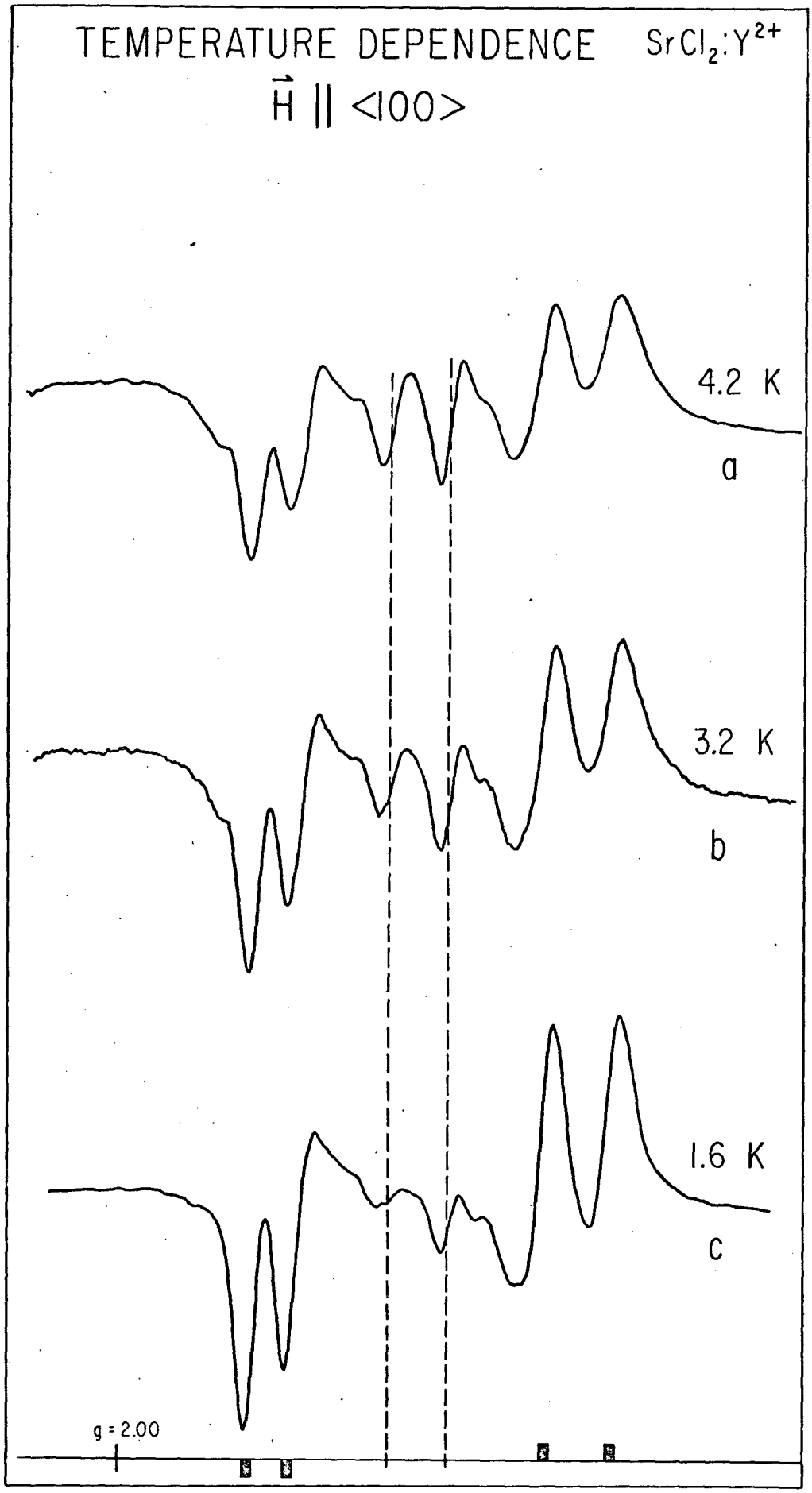
TEMPERATURE DEPENDENCE $SrCl_2:Y^{2+}$
$\vec{H} \parallel \langle 100 \rangle$
4.2 K
a
3.2 K
b
1.6 K
c
g = 2.00
MAGNETIC FIELD →
= 40 GAUSS

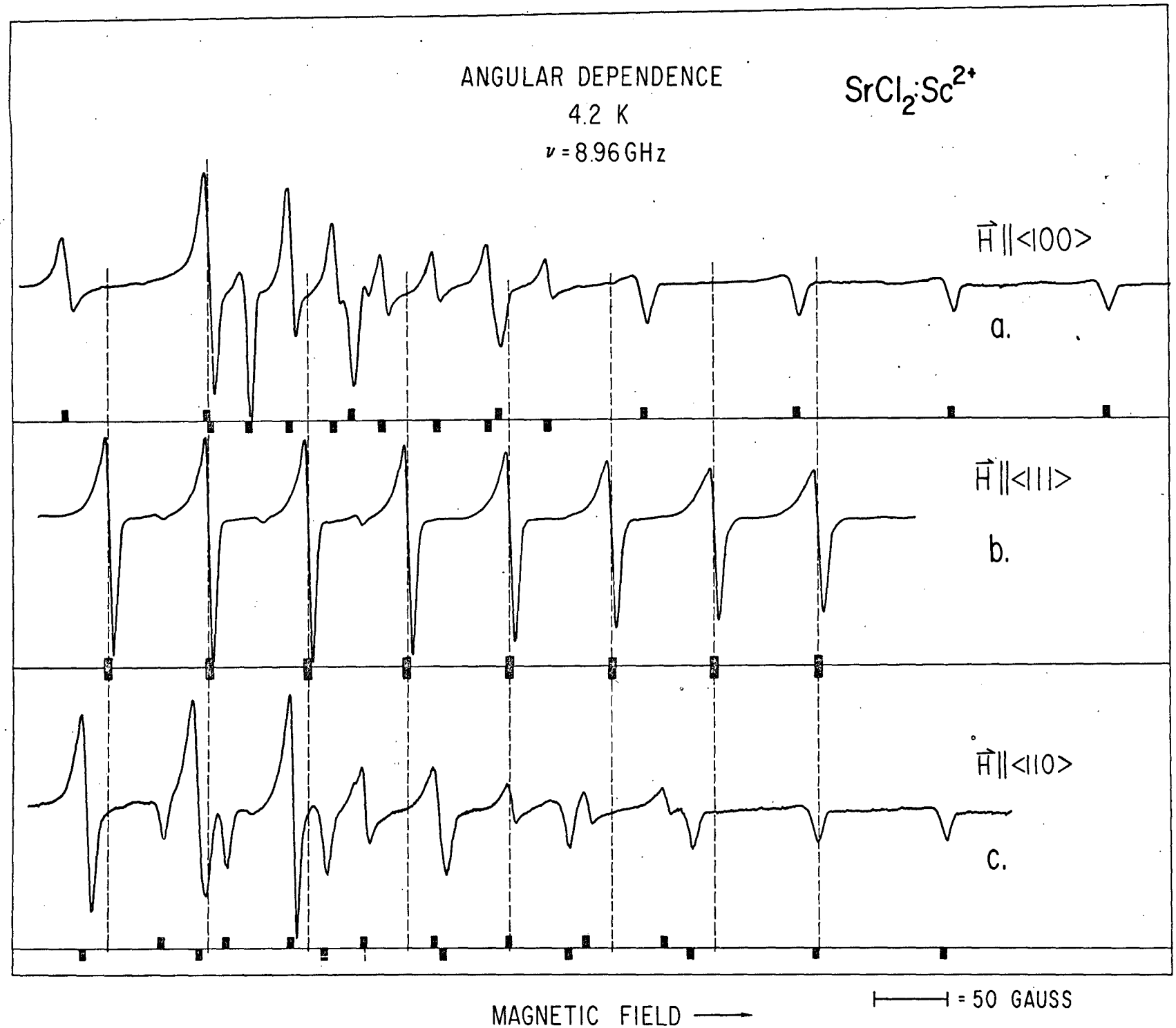
ANGULAR DEPENDENCE
4.2 K
ν = 8.96 GHz
SrCl2:Sc2+
H||<100>
a.
H||<111>
b.
H||<110>
c.
MAGNETIC FIELD
= 50 GAUSS

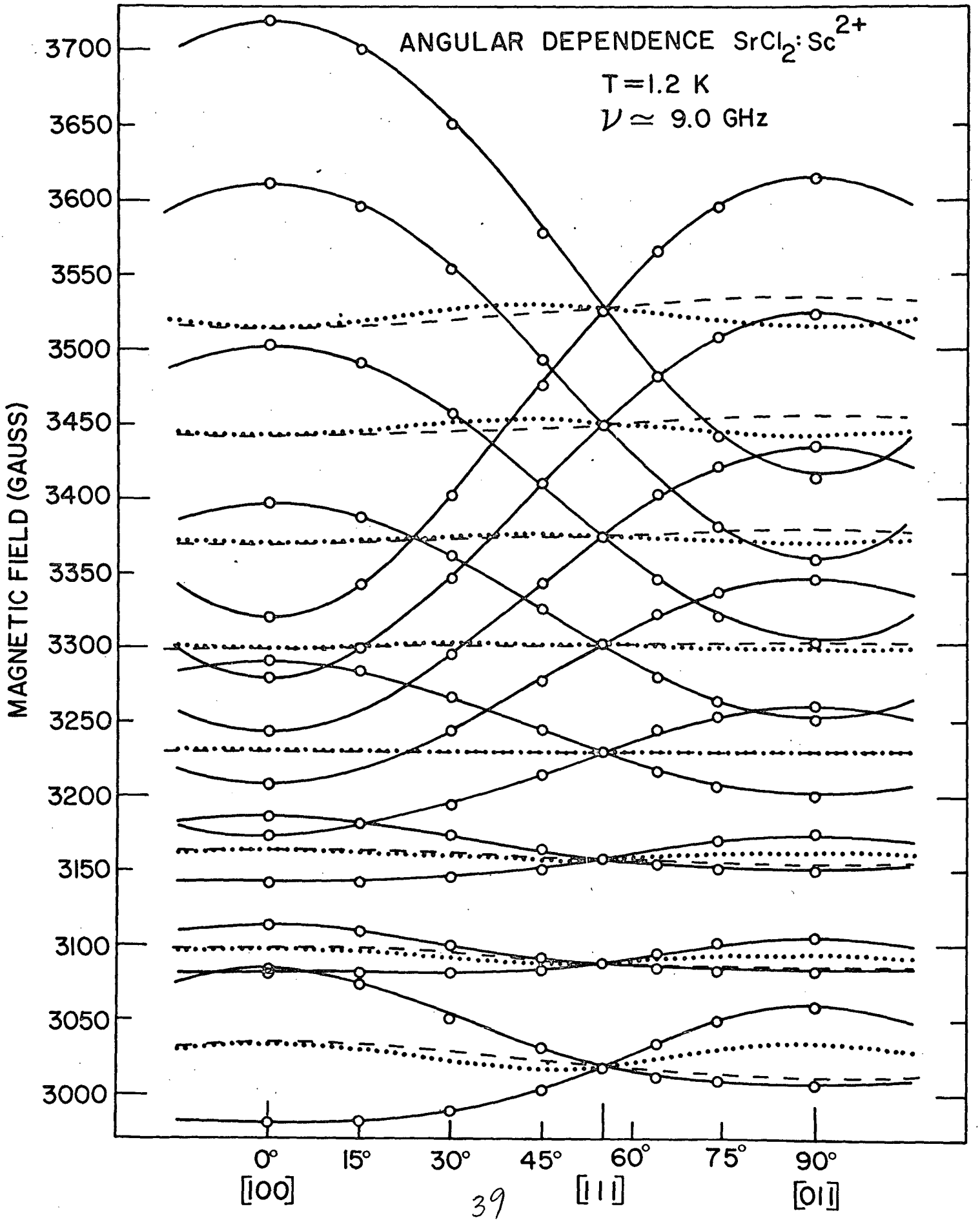
ANGULAR DEPENDENCE $SrCl_2:Sc^{2+}$
T=1.2 K
$\nu \simeq$ 9.0 GHz
MAGNETIC FIELD (GAUSS)
3700
3650
3600
3550
3500
3450
3400
3350
3300
3250
3200
3150
3100
3050
3000
0°
15°
30°
45°
60°
75°
90°
[100]
[11]
[011]

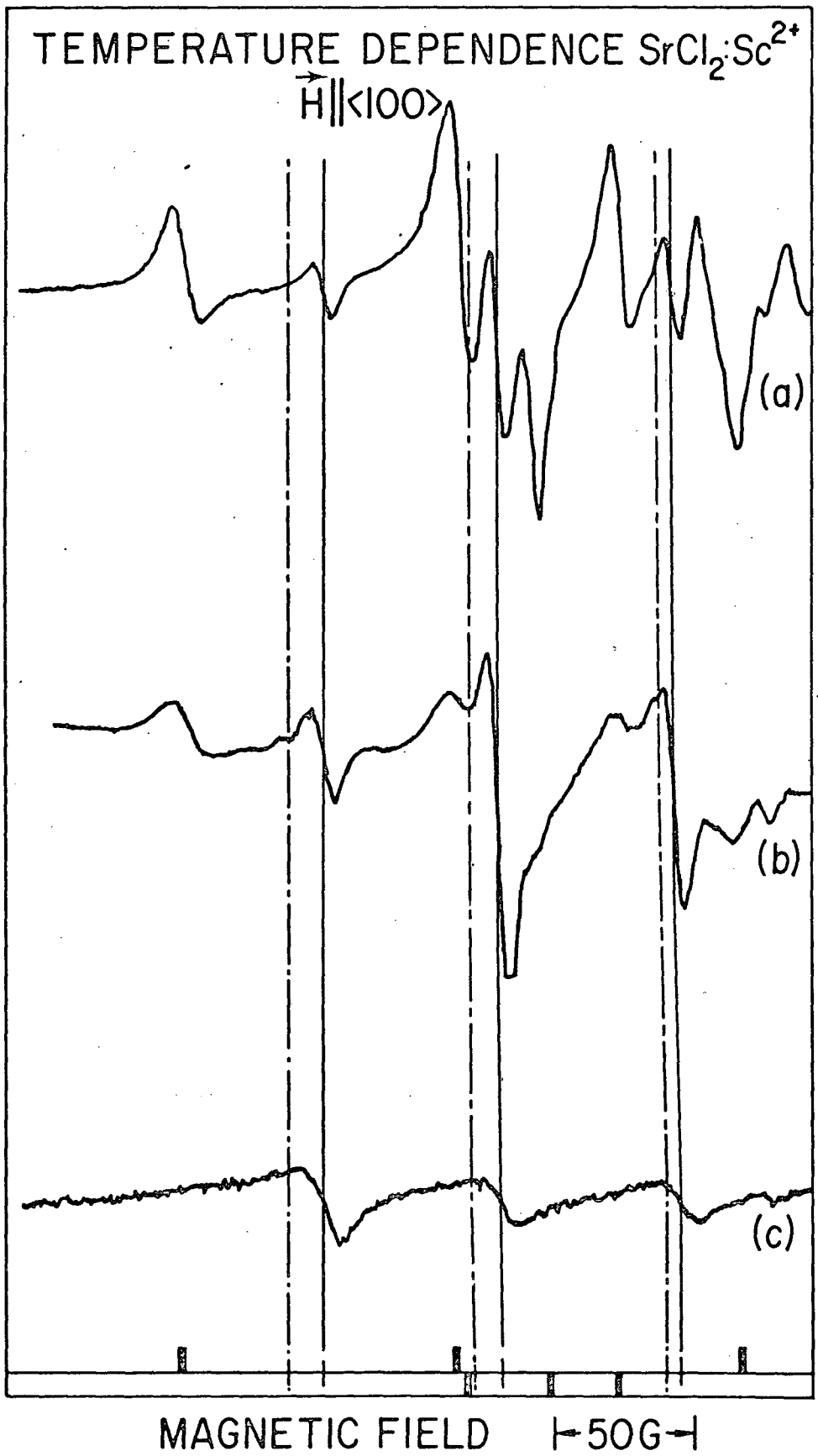
TEMPERATURE DEPENDENCE $SrCl_2:Sc^{2+}$
$\vec{H} \| \langle 100 \rangle$
(a)
(b)
(c)
MAGNETIC FIELD
50G

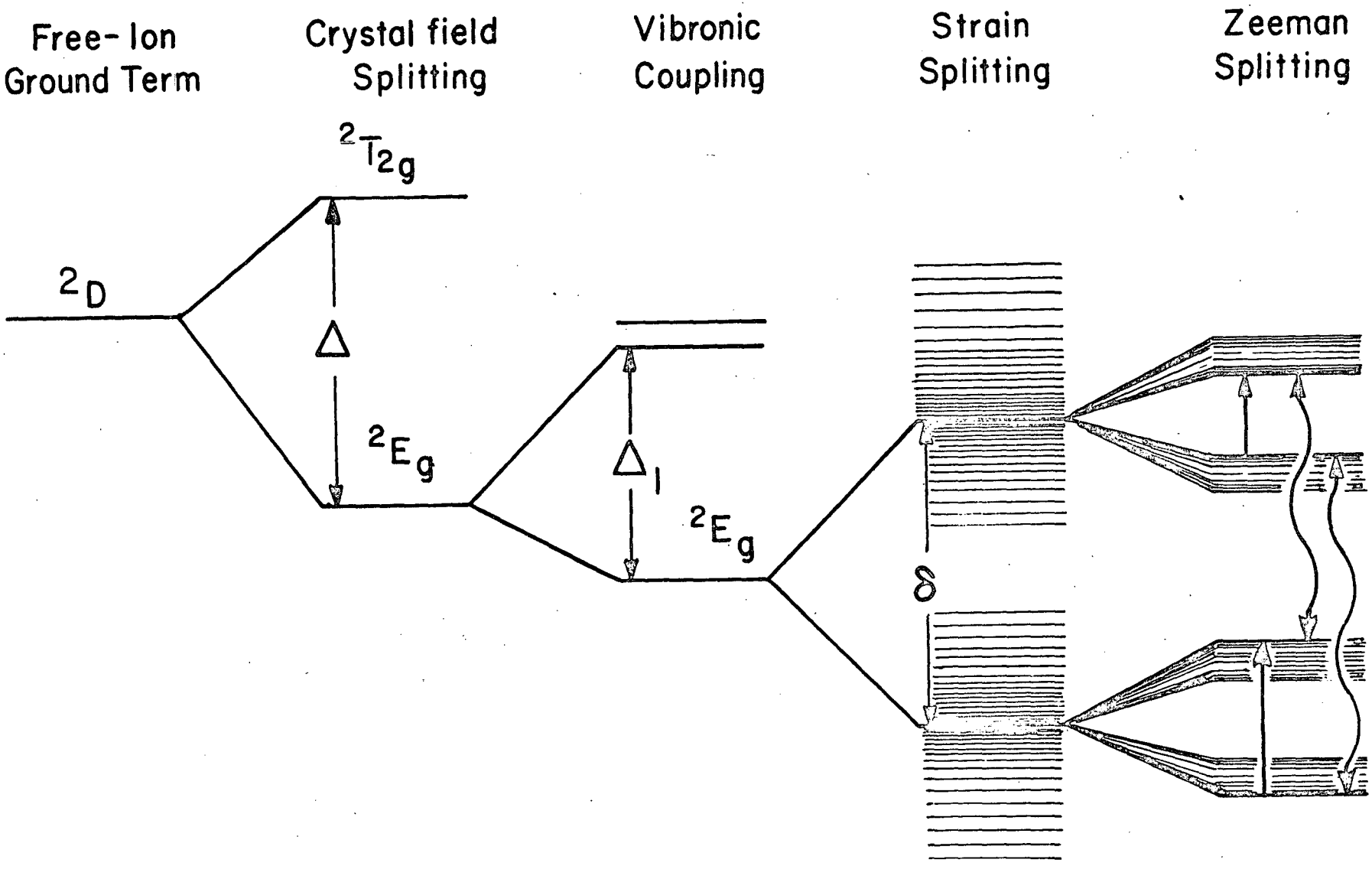
Free-Ion Ground Term
Crystal field Splitting
Vibronic Coupling
Strain Splitting
Zeeman Splitting
$^2T_{2g}$
^2D
Δ
^2E_g
Δ_1
^2E_g
δ